



OPEN

Efficacy of atomic layer deposition of Al_2O_3 on composite $\text{LiNi}_{0.8}\text{Mn}_{0.1}\text{Co}_{0.1}\text{O}_2$ electrode for Li-ion batteries

Heran Huang¹, Linna Qiao¹, Hui Zhou¹, Yalun Tang², Matthew J. Wahila³, Haodong Liu⁴, Ping Liu⁴, Guangwen Zhou^{1,5}, Manuel Smeu^{1,6} & Hao Liu^{1,7}✉

$\text{LiNi}_{0.8}\text{Mn}_{0.1}\text{Co}_{0.1}\text{O}_2$ (NMC811) is a popular cathode material for Li-ion batteries, yet degradation and side reactions at the cathode-electrolyte interface pose significant challenges to their long-term cycling stability. Coating $\text{LiNi}_x\text{Mn}_y\text{Co}_{1-x-y}\text{O}_2$ (NMC) with refractory materials has been widely used to improve the stability of the cathode-electrolyte interface, but mixed results have been reported for Al_2O_3 coatings of the Ni-rich NMC811 materials. To elucidate the role and effect of the Al_2O_3 coating, we have coated commercial-grade NMC811 electrodes with Al_2O_3 by the atomic layer deposition (ALD) technique. Through a systematic investigation of the long-term cycling stability at different upper cutoff voltages, the stability against ambient storage, the rate capability, and the charger transfer kinetics, our results show no significant differences between the Al_2O_3 -coated and the bare (uncoated) electrodes. This highlights the contentious role of Al_2O_3 coating on Ni-rich NMC cathodes and calls into question the benefits of coating on commercial-grade electrodes.

The layered lithium transition metal oxide with the general formula of $\text{LiNi}_x\text{Mn}_y\text{Co}_{1-x-y}\text{O}_2$ (NMC) forms an important family of cathode materials for Li-ion batteries thanks to their high theoretical capacity, energy density, and tunable chemical composition. Recent efforts to increase the Ni concentration at the expense of Co have led to the Ni-rich NMC materials, epitomized by the state-of-the-art $\text{LiNi}_{0.8}\text{Mn}_{0.1}\text{Co}_{0.1}\text{O}_2$ (NMC811), which is widely adopted in commercial Li-ion battery cells. However, the reversible capacity reported for Ni-rich NMC cathodes corresponds to only ~80% of their theoretical capacity because significant degradations occur at a higher capacity utilization (i.e., a higher upper cut-off voltage). One major cause of the capacity degradation is the instability at the NMC cathode surface, which has been found to undergo irreversible structural reconstruction^{1–4}, oxygen evolution^{5–8}, transition metal ion dissolution^{4,9–11}, and the electrolyte decomposition^{12–15}. This surface degradation also aggravates the electrolyte decomposition, which inevitably occurs at high reduction potentials^{16–25}. The prevailing consensus is that a stable cathode-electrolyte interface is important to enable high-voltage cycling. Strategies to increase this interfacial stability include elemental substitution and doping^{7,16,26–29}, concentration gradient in cathode particles^{30–35}, surface coating and modification^{3,14,26,27,36–42}, and electrolyte formulation^{43,44}.

Surface coating provides a direct method to tailor the chemical and physical properties of the electrode surface, thereby modifying the electrode's stability against the electrolyte. The coating layer has been proposed to act as a physical barrier between the cathode and the electrolyte to stabilize the cathode-electrolyte interface and/or as an HF scavenger to disrupt the autocatalytic hydrolysis of the LiPF_6 electrolyte salt^{9,45}. A variety of methods are available to modify the electrode surface, which includes surface coating via high-temperature heat treatment³⁷, liquid phase deposition^{38,40,46–49}, atomic layer deposition (ALD)^{3,38,41,50–54}, facing-target sputtering (FTS)⁵⁵, metallurgy⁵⁶, mechanochemistry^{57,58}, and a combination of these methods⁴¹. Amongst these, the ALD method is especially appealing as it allows the controlled and conformal growth of the coating layer with diverse chemistry at moderate temperatures⁵⁹. The ALD can be applied to both electrode films^{36,51,60} and active

¹Materials Science and Engineering, Binghamton University, Binghamton, NY 13902-6000, USA. ²Department of Electrical and Computer Engineering, University of California San Diego, 9500 Gilman Drive, La Jolla, CA 92093, USA. ³Analytical and Diagnostics Lab, Binghamton University, Binghamton, NY 13902-6000, USA. ⁴Department of NanoEngineering, University of California San Diego, La Jolla, CA 92093, USA. ⁵Department of Mechanical Engineering, Binghamton University, Binghamton, NY 13902-6000, USA. ⁶Department of Physics, Applied Physics and Astronomy, Binghamton University, Binghamton, NY 13902-6000, USA. ⁷Department of Chemistry, Binghamton University, Binghamton, NY 13902-6000, USA. ✉email: liuh@binghamton.edu

material powders^{38,41,48}. Refractory materials, such as ZrO_2 and Al_2O_3 , are commonly used for surface coatings. For example, coating NMC811 powder with layers of ZrO_2 ^{41,62} or Al_2O_3 ^{14,41,51,60} via ALD have resulted in improved the long-term capacity retention. Annealing of the coated NMC811 powders has been found to reduce the polarization and increase the specific capacity, Coulombic efficiency, and the rate capability^{41,62}. However, recent studies of NMC811 powders coated by Al_2O_3 using wet chemical methods showed a nuanced or even detrimental⁶³ effect of annealing on the capacity retention⁶⁴.

Direct coating of composite electrode films via ALD has also been adopted to improve the electrochemical performance^{1,3,14,51,60,61,65} because the coating has been proposed to protect all exposed surfaces, including those from both the active cathode material and carbon black additives, from direct contact with electrolyte^{66,67}. For example, improved capacity retention has been reported for a series of NMC532⁶⁰, NMC622⁵¹, and NMC811¹⁴ composite electrodes coated with Al_2O_3 by ALD. However, these coating studies are based either on home-made cathode materials which present inferior performance to their commercial counterparts or on NMC with less nickel content (e.g. NMC532 and NMC622). This begs the question of whether coating on commercial-grade NMC811 electrode would still be effective in improving the electrochemical performance. While uniform and conformal coating can be achieved by ALD on cathode powders, the homogeneity of the coating via ALD on electrodes has not been studied. Therefore, investigation of the coating via ALD on commercial-grade electrodes is needed to guide their application in practical battery electrodes.

Here, we present a systematic investigation of the effect of Al_2O_3 coating by the ALD technique on commercial-grade NMC811 electrodes. We examined the effect of the Al_2O_3 coating thickness, modulated by the number of ALD cycles, on the long-term cycling performance at different cut-off voltages, the electrode's stability against ambient exposure, and the rate capability. No significant differences are observed between the coated and the bare electrodes. Our result questions the efficacy of direct coating on Ni-rich NMC electrodes when the active electrode materials are optimized.

Results

Characterization of commercial NMC811 powder

Figure 1a and b show the SEM images of the as-received commercial NMC811 powder, which consists of spherical secondary particles with a median diameter of 15 μm . Elemental analysis by EDX was performed to examine potential surface coating and/or doping that could be present in commercial NMC811 powders. The EDX spectrum (Fig. 1c) shows no peaks other than those from Ni, Mn, Co and O, ruling out the presence of substantial surface coating or doping in this batch of NMC811 powder. EDX result also shows the atomic ratio of Ni:Mn:Co in this sample is 8.00:0.90:1.03, which agrees well with the nominal ratio of 8:1:1.

Surface characterization of electrodes coated by Al_2O_3 via ALD

The as-received NMC811 powders were prepared into homogeneous electrodes with an areal loading of 5.6 mg/cm². Electrodes from the same batch were further coated with Al_2O_3 via ALD. ALD with 2, 5, 10, and 20 cycles were applied to the electrodes to yield different coating layer thicknesses, which are denoted as ALD-2, ALD-5,

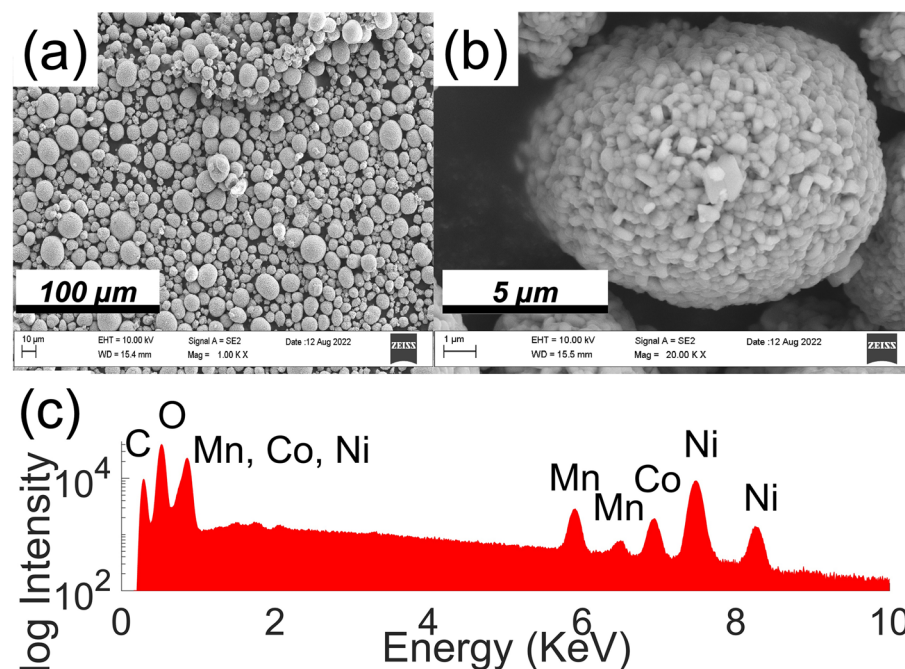


Figure 1. (a, b) Scanning electron microscopy images of the commercial NMC811 powder. (c) EDX spectrum of the as-received commercial NMC811 powders. Vertical axis plotted on logarithmic scale.

ALD-10 and ALD-20, respectively. The XRD pattern indicates the preservation of NMC811 layered structure after 20 cycles of ALD repetitions (Supplementary Fig. S1). The Al 2p XPS spectra were measured for all the electrodes to validate the presence of Al₂O₃ coating after ALD (Fig. 2a). No Al 2p peak is observed for the bare NMC811 electrode, which is consistent with the EDX result. An Al 2p peak at 75.00 eV is observed for all electrodes coated via ALD and is assigned to Al₂O₃⁶⁸. The integrated area of the Al 2p peak increases linearly with the number of ALD cycles (Fig. 2b), which suggests the growing thickness of the Al₂O₃ coating layer with increasing ALD cycles. This is consistent with the layer-by-layer deposition mechanism of ALD.

HAADF-STEM and EDX mapping was used to examine the Al₂O₃ coating introduced by the ALD method. A weak Al intensity is observed on the surface of the secondary NMC811 particle from the ALD-2 electrode (Fig. 3a), whereas a strong and continuous Al intensity covers the surface of the secondary NMC811 particle from the ALD-20 electrode (Fig. 3b). The EDX mapping result indicates the growing Al content on the NMC particle surface with increasing ALD cycles. Accordingly, TEM images of the surface region of the NMC particles show a thicker deposition layer in the ALD-20 (Fig. 3d) than ALD-2 (Fig. 3c) sample. This electron microscopy result is consistent with the XPS result (Fig. 2) and demonstrates the growing thickness of the Al₂O₃ coating layer with increasing ALD cycles.

Electrochemical performance at room temperature

Electrochemical cycling was conducted to examine the effect of the Al₂O₃ coating via ALD on the cycling stability against different upper cut-off voltages at 4.4 V and 4.6 V. Figure 4a shows the specific capacity over 100 cycles at 4.4 V upper cut-off voltage. Both the bare and the coated electrodes exhibit a starting capacity of 200 mAh/g, which is typically observed for NMC811 electrodes at this cut-off voltage^{7,69}. After 100 cycles, the discharge capacity decreases to ~160 mAh/g with no significant differences between the coated and bare electrodes. This capacity degradation agrees well with a previous report of ~157 mAh/g after 100 cycles for a Ni-rich LiNi_{0.83}Mn_{0.05}Co_{0.12}O₂ electrode⁷⁰. No significant difference in the Coulombic efficiency is observed. Based on the numerical data provided by the statistical analysis of NMC811 electrodes by Savina et al.⁷¹, the median capacity decay rate is 0.135% per cycle for 48 studies with an upper cutoff voltage of 4.4 V. The decay rate of 0.2% per cycle in the present study is lower than 14 (out of 48) other studies. However, of the 6 studies using commercial NMC811 materials (Table S1), only 2 studies by Xin et al.²⁷ and Thapalia et al.⁷² reported a lower capacity decay rate than ours. In the study by Xin et al., the electrode was calendered, which has been shown to increase the capacity retention for Ni-rich NMC electrodes⁷³. In the study by Thapalia et al., the first-cycle capacity for 4.4 V cycling was 180 mAh/g, which corresponds to a lower state of charge than the present work at the end of charge. Since the equilibrium state of charge at 4.4 V is the onset potential for the detrimental gas release and surface reconstruction reactions^{74,75}, a lower state of charge is expected to result in a lower rate of capacity decay. Therefore, the capacity decay rate in the present work is consistent with existing literature on commercial NMC811 electrodes⁷⁶.

For the long-term cycling at the upper cut-off voltage of 4.6 V, two identical cells were prepared and measured for each electrode sample. The average discharge capacity and Coulombic efficiency are shown in Fig. 4b, where the error bars indicate the difference in capacity between the two identical cells. An initial specific discharge capacity of 215 mAh/g is observed for both the coated and the bare electrodes, which is slightly higher than the previously reported value of ~205 mAh/g at the same cut-off voltage²⁷. Again, there is no significant difference

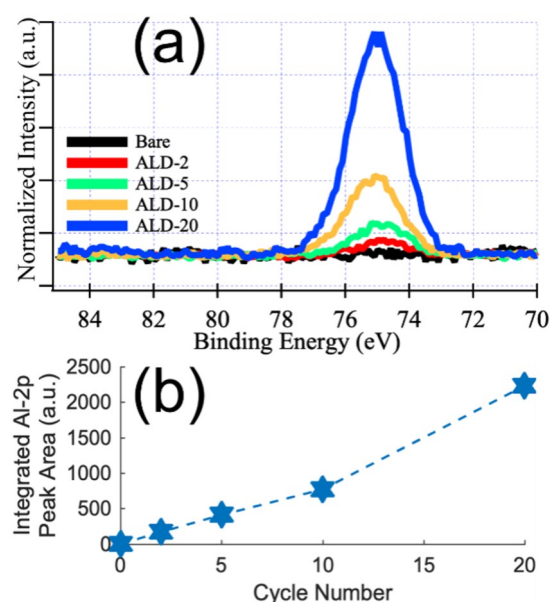


Figure 2. (a) Normalized Al-2p XPS spectra measured for bare and coated electrodes. (b) The integrated area of the Al-2p peaks as a function of the ALD cycle number.

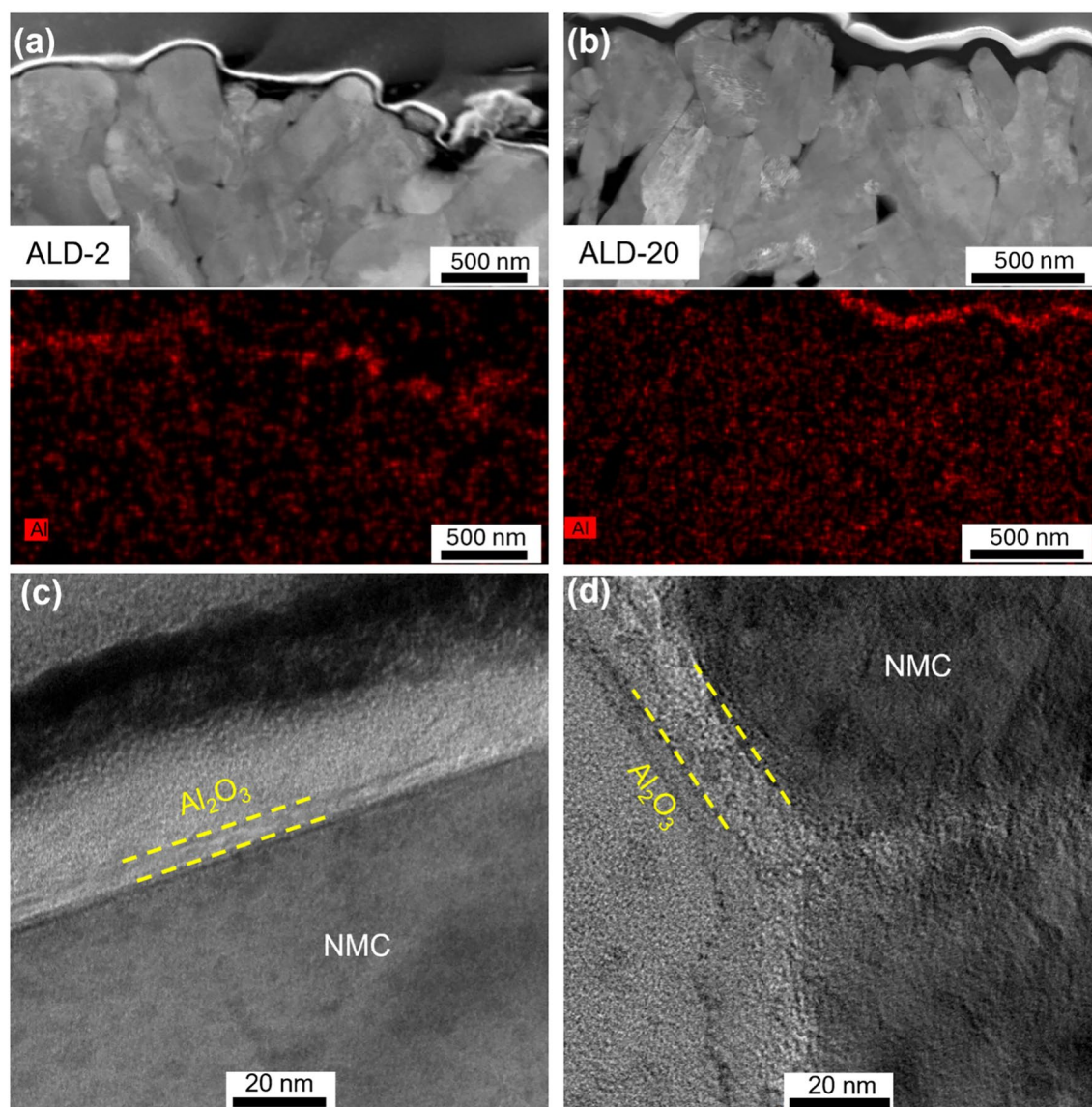


Figure 3. (a, b) HAADF-STEM and EDX Al mapping of the FIB slice prepared from the NMC811 electrode coated by 2 and 20 ALD cycles, respectively. (c, d) TEM images of the surface region for the ALD-2 and ALD-20 electrode, respectively.

in the Coulombic efficiency between the bare and the coated electrodes. The standard deviation of the measured specific capacity, as indicated by error bars in Fig. 4b, of all five samples is ~ 2 mAh/g for the 1st cycle, which demonstrates the high consistency in the electrode preparation and ALD coating. However, the standard deviation increases with the cycle number and reaches ~ 10 mAh/g at the 100th cycle.

To examine the effect of Al₂O₃ coating on the voltage polarization, the voltage profiles for all samples at select cycles are plotted in Fig. 5. Figure 5a shows the 1st cycle voltage profiles of both the bare and the coated electrode samples cycled with 4.4 V cutoff. All five samples are initially onset to a higher open-circuit voltage, which is probably caused by different coating thicknesses and unpredictable surface species synergistically. Nevertheless, all five electrode samples yield a close specific charge capacity of 233 mAh/g and nearly identical voltage profiles during discharge regardless of the coating thickness. In comparison, previous reports for NMC811 particles^{15,40,41} with Al₂O₃ coating^{40,41} showed in a slight decrease of 2–8 mAh/g in the specific discharge capacity. After 100 cycles, substantial changes in the voltage profile are observed for both the bare and the coated electrodes (Fig. 5b): the capacity of the constant voltage charging step at 4.4 V increases to ~ 18 mAh/g, as opposed to ~ 5 mAh/g in the 1st cycle, which is attributed to the increased voltage polarization after long-term cycling. The specific discharge capacity decreases to ~ 160 mAh/g for all electrodes, regardless of the coating thickness. This shows that the Al₂O₃ coating on electrodes does not suppress the voltage or the capacity decay at least for the first 100 cycles with a cutoff voltage of 4.4 V under room temperature.

Comparison in the evolution of the voltage profile was also made for electrodes cycled with the upper cutoff voltage of 4.6 V (Fig. 5c and d). For the first cycle, all five samples show a similar onset voltage with unnoticeable difference as well as their charge and discharge capacities. After 100 cycles, the voltage polarization for cycling

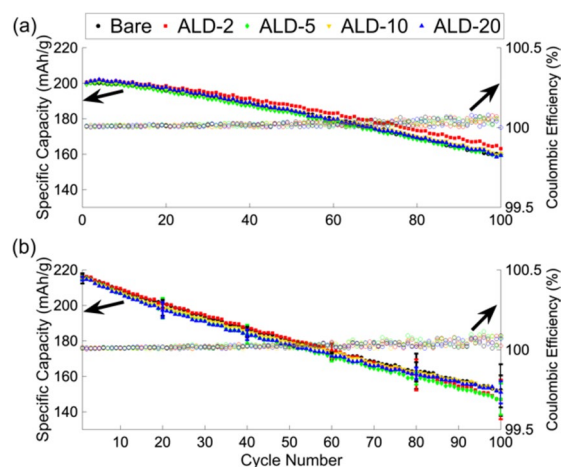


Figure 4. Specific discharge capacity of both the bare and the coated electrodes cycled with an upper cutoff voltage of (a) 4.4 V and (b) 4.6 V. Error bars correspond to the differences in capacity between the two replicate measurements for the 4.6 V samples and are shown for every 20 cycles.

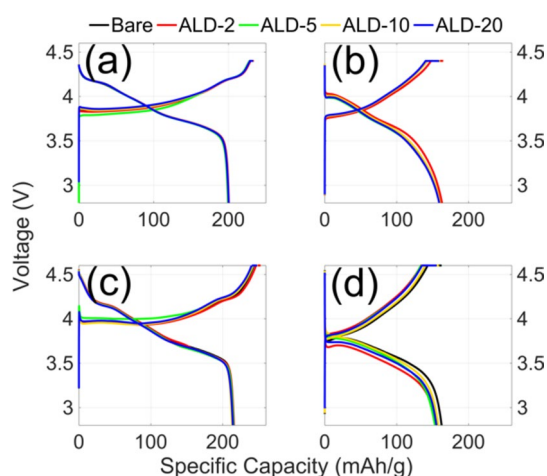


Figure 5. Voltage profiles of (a) the first and (b) the 100th cycles for the electrodes cycled within the voltage window of 2.8–4.4 V, and the voltage profiles of (c) the first and (d) the 100th cycles for the electrodes cycled within the voltage window of 2.8–4.6 V.

at 4.6 V is increases by ~ 181 mV than cycling at the 4.4 V (as shown in Supplementary Fig. S2). The capacity for the constant voltage charging step increases to ~ 20 mAh/g, and the specific discharge capacity decreases to 153–163 mAh/g for all electrodes regardless of the coating thickness. Again, no significant difference in the capacity retention or voltage polarization is observed for the bare and the coated electrodes. Therefore, the Al_2O_3 coating on electrodes does not improve the capacity retention nor reduce the voltage polarization for cycling with upper cutoff voltages of up to 4.6 V.

Stability against air exposure

To explore whether the Al_2O_3 coating increases the stability of the electrode against moisture exposure, both the coated and the bare electrodes were exposed to air (43% relative humidity, 22 °C) for 1 day and 30 days before electrochemical cycling. The specific discharge capacity for the first 100 cycles of the 1-day and 30-day exposed samples is shown in Figs. 6a and 7a, respectively. After 1-day exposure, the bare electrode shows a small but noticeable drop in the initial specific discharge capacity to 195 mAh/g, as opposed to ~ 200 mAh/g observed for non-exposed electrode (Fig. 4a). This observation is in agreement with the report by Sicklinger et al.⁷⁷, where a drop in the initial specific capacity is observed for electrodes after long-term storage in inert dry atmosphere and after short-term storage in a high-humidity environment. In contrast, no drop in the initial discharge capacity is observed for any of the coated electrodes. The voltage polarizations of all four coated electrodes stay nearly the same with the bare electrode as shown in Supplementary Fig. S3a. After 100 cycles, the bare electrode retains a capacity of 153 ± 5 mAh/g, whereas the coated electrodes retain a slightly higher capacity of 160 ± 6 mAh/g regardless of the coating thickness (Fig. 6a). Among all the coated electrodes, only the ALD-20 electrode shows a smaller voltage polarization than the bare electrode, especially in the high-voltage regime (Supplementary

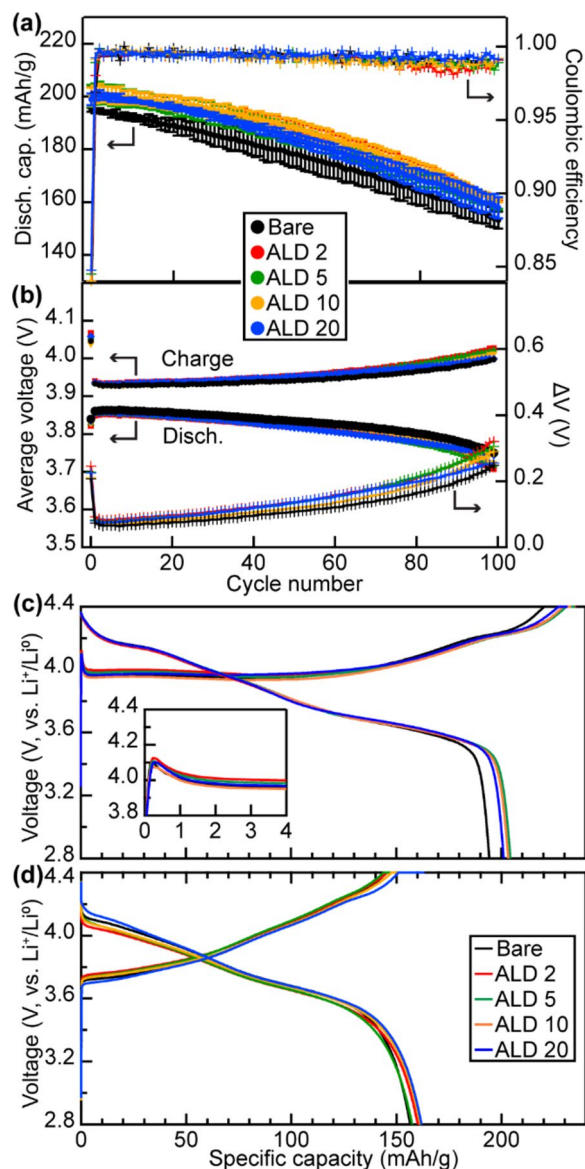


Figure 6. Electrochemical behavior of both the bare and the coated electrodes after 1-day air exposure: (a) Specific discharge capacity, (b) average charge/discharge voltages and the voltage polarization (ΔV) for 100 cycles, and the voltage profiles for (c) the 1st cycle and (d) the 100th cycle. The electrodes were cycled at C/3 rate, and the specific discharge capacity is averaged over two parallel measurements. The error bars indicate the difference between the results from the two parallel experiments.

Fig. S3b). Although all coated electrode samples started off and ended up with higher capacities than the bare electrode after 1-day exposure, a capacity drop of ~ 40 mAh/g after 100 cycles is observed for both the bare and the coated samples (e.g., capacity drops of 42 ± 5 mAh/g, 39.7 ± 0.5 mAh/g, 42.9 ± 0.2 mAh/g, 39.2 ± 0.9 mAh/g and 41 ± 6 mAh/g are observed for the bare, ALD-2, ALD-5, ALD-10 and ALD-20 electrodes, respectively, after 100 cycles). The average voltage (i.e., specific energy/specific capacity) is calculated to examine the effect of Al_2O_3 coating on the evolution of the voltage polarization (Fig. 6b). The average charge voltage for the 1st cycle is 4.05 V, which contributes to the large voltage polarization (i.e., difference between average charge and discharge voltages, denoted as ΔV) observed for the 1st cycle. The average charge voltage drops to 3.93 V in the 2nd cycle and gradually increases to 4 V in the 100th cycle. The average voltage polarization (ΔV) increases from 0.07 V for the 2nd cycle to 0.25–0.32 V for the 100th cycle with no significant differences between the coated and the bare electrodes (Fig. 6b). Examination of the 1st cycle voltage profile shows voltage spike at the beginning of charge followed by a long voltage plateau at 4 V (Fig. 6c). Such a voltage profile is commonly observed for electrodes exposed to air⁷⁸ and has been attributed to the decomposition of surface carbonate species introduced as a result of the air exposure⁷⁹. This voltage polarization is absent during the subsequent discharge step and in later cycles (Fig. 6d).

For electrodes exposed to air for 30 days, an initial discharge capacity of 191–197 mAh/g is observed for both the coated and the bare electrodes (Fig. 7a), which is comparable to the non-exposed and 1-day exposed

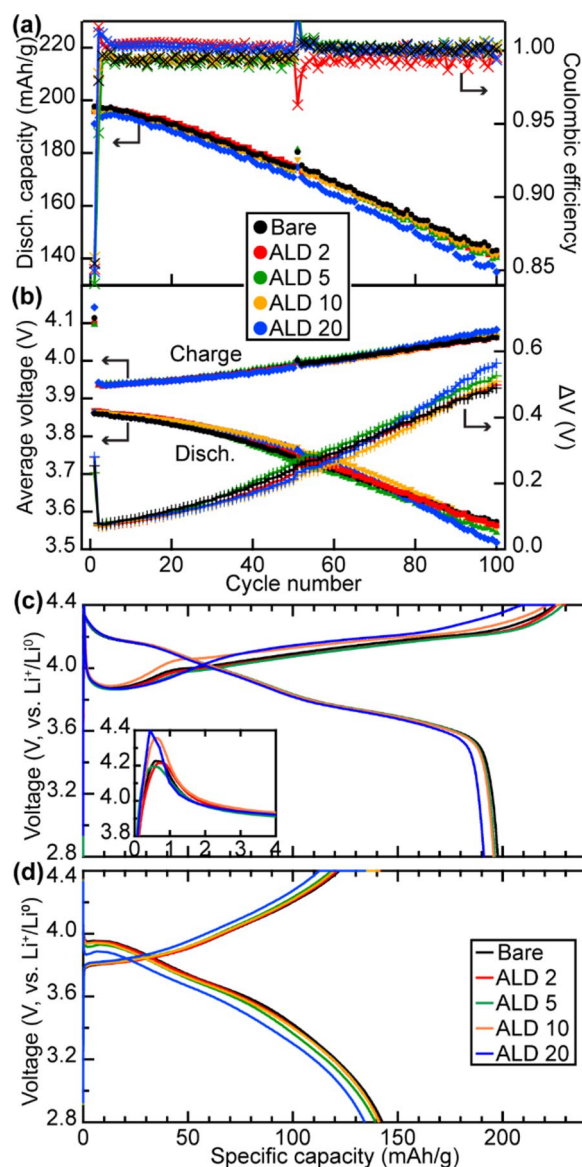


Figure 7. Electrochemical behavior of both the bare and the coated electrodes after 30-day air exposure: (a) Specific discharge capacity, (b) average charge/discharge voltages and the voltage polarization (ΔV) for 100 cycles, and the voltage profiles for (c) the 1st cycle and (d) the 100th cycle. The electrodes were cycled at C/3 rate.

electrodes. However, the discharge capacity for both the coated and the bare electrodes after 30-day exposure drops to ~ 140 mAh/g in the 100th cycle, which is much lower than that of the non-exposed electrodes (~ 160 mAh/g) and the 1-day moisture exposed electrodes (~ 160 mAh/g). This shows the accelerated capacity degradation with prolonged air exposure. Calculation of the average voltage shows a higher average charge voltage of ~ 4.1 V and a larger voltage polarization than the 1-day exposed electrodes for the 1st cycle; the average voltages and the voltage polarization for the 2nd cycle are similar for both the 1-day and the 30-day exposed electrodes (Fig. 7b). Nevertheless, the voltage polarization for the 30-day exposed electrodes increases to 0.5 V as opposed to 0.3 V for the 1-day exposed electrodes at the 100th cycle. Again, no significant difference is observed between the coated and the bare electrodes. Examination of the voltage profile reveals an increased voltage spike at the beginning of the initial charge, indicating a more prominent growth of surface impurities than the 1-day exposed electrodes (Fig. 7c). Accordingly, the voltage polarization becomes more aggravated for the 30-day exposed than the 1-day exposed electrodes in the 100th cycle (Fig. 7d).

Kinetics studies

To investigate the effect of Al_2O_3 coating on the rate capability, two parallel rate tests were performed for the coated and the bare electrodes (Fig. 8). Yet, no significant differences in the discharge capacity are observed for discharge rate up to 3C.

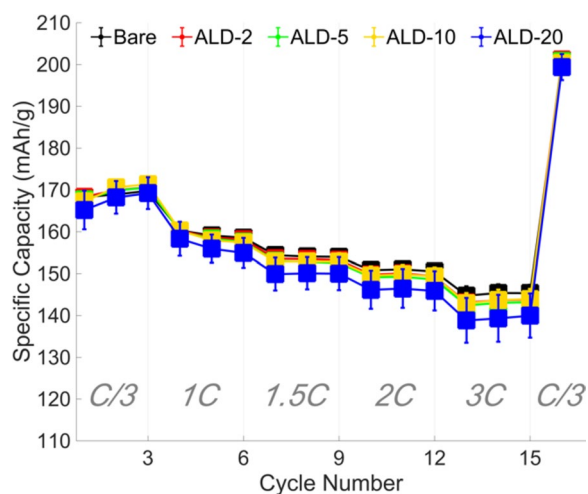


Figure 8. Specific discharge capacity obtained at different discharge rates. Cycling was performed in the voltage window of 2.8–4.2 V, and the CCCV charging protocol at C/3 was applied while only varying the discharge rate from C/3, 1 C, 1.5 C, 2 C and 3 C. One more charge–discharge cycle at C/3 rate and cutoff up to 4.4 V is appended at the end of rate test to show the preservation of sample after the rate test.

PITT was also introduced to quantify the Li-ion diffusivity and the exchange current density of the coated and bare electrode samples (the entire PITT voltage profiles are shown in Supplementary Fig. S4). To eliminate the uncertainties related to the measurement of the particle size in the determination of the Li-ion diffusivity, the quotient of D/r^2 is reported in Fig. 9a. The shape of the D/r^2 curve is similar to our previous measurement for a single-crystalline NMC electrode²⁶ and other reports for NMC811 cathodes^{80–82}. No significant difference in the Li-ion diffusivity is observed between all samples. This is consistent with our expectation that the surface coating does not affect the bulk Li-ion diffusivity. To calculate the exchange current density (j_0), a radius of $r = 0.5 \mu\text{m}$ is assumed for the primary particle size of the NMC811 powder (Fig. 9b). The exchange current density is on the order of 0.1 mA/cm^2 and increases with voltage, which is consistent with a previous measurement for isolated NMC811 secondary particles⁸². However, no systematic differences are observed between the coated and the electrodes. This result shows that coating on the electrode does not change the intrinsic kinetic properties of the NMC811 particles.

Electrochemical impedance spectroscopy (EIS) measurement was used to interrogate changes in the electrode surface between the bare and the coated electrodes. Figure 10a shows the Nyquist plots measured for electrodes

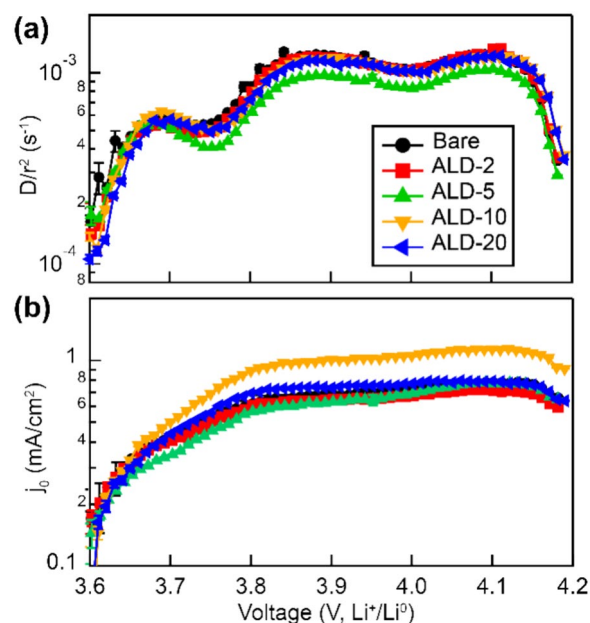


Figure 9. (a) D/r^2 and (b) j_0 obtained from fitting the PITT results. D , r , and j_0 correspond to the Li diffusivity, radius of the NMC811 particle, and the exchange current density, respectively.

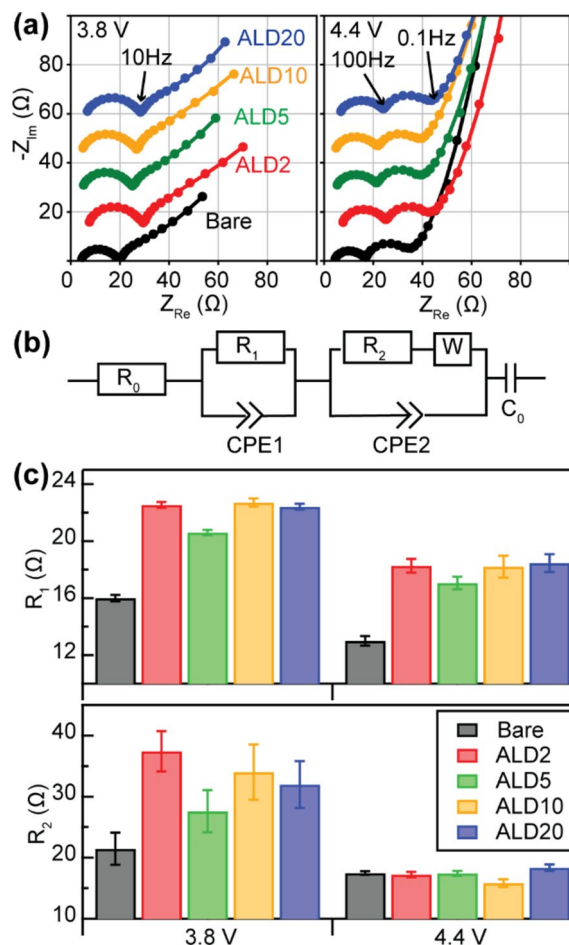


Figure 10. (a) Electrochemical impedance spectra measured for the bare and the Al₂O₃-coated electrodes at 3.8 V and 4.4 V during the first charge. A vertical offset of 15 Ω is applied between consecutive curves. Experimental data and the fitting curves are represented by solid circles and lines, respectively. (b) Equivalent circuit model used to fit the experimental EIS results. (c) Surface layer resistance (R_1) and charge-transfer resistance (R_2) obtained from the equivalent circuit modeling of the EIS spectra.

charged to 3.8 V and 4.4 V on the first charge. At 3.8 V, the Nyquist plot exhibits a well-defined semicircle arc at frequencies above 10 Hz, a suppressed semicircle at lower frequencies, and low-frequency linear region for both bare and coated electrodes. This suppressed semicircle becomes much better defined between 100 Hz and 0.1 Hz for all electrodes at 4.4 V. The growing prominence of the mid-frequency arc with increasing voltage is in agreement with previous EIS studies of NMC811 electrodes⁸⁰. It is well established that the high-frequency semicircle is related to the surface film formed on the electrode and mid-frequency semicircle is related to the charge transfer at the electrode–electrolyte interface. To model the EIS result, we have employed the equivalent circuit model adopted by Trevisanello et al.⁸³ (Fig. 10b), where R_0 , R_1 , and R_2 correspond to the bulk resistance of cell, the resistance of the surface film on the electrode, and the charge-transfer resistance, respectively. Figure 10c shows the fitting results. The surface layer resistance (R_1) for the coated electrodes (20–22 Ω at 3.8 V and 17–18 Ω at 4.4 V) is consistently larger than for the bare electrodes (16 Ω at 3.8 V and 13 Ω at 4.4 V). The increased surface layer resistance for the coated electrode is attributed to the Al₂O₃ coating layered introduced by the ALD. However, the R_1 is effectively independent of the Al₂O₃ layer thickness^{27,80,84}. While the charge transfer resistance (R_2) for the coated electrode (27–37 Ω) is consistently larger than the bare electrode (21 Ω) at 3.8 V, the R_2 becomes effectively identical for both coated and bare electrodes at 4.4 V. It is worth pointing out that the fitting result for R_2 is more robust at 4.4 V, where the mid-frequency semicircle is much better resolved and the estimated errors of the fitting results are smaller than at 3.8 V. This shows that the charge transfer resistance is not affected by the Al₂O₃ coating layer.

In comparison, past studies on the coating of NMC electrode films often lack systematic characterization of the kinetic properties of the coated electrode and leads to mixed results. For example, Su et al. reported a slight decrease in the Li-ion diffusivity when the NMC532 electrode film was coated with Al₂O₃ via 5 and 10 ALD cycles³; yet the diffusivity was found by Shi et al. to increase by an order of magnitude for an NMC532 electrode coated with Al₂O₃ via 4 ALD cycles⁶⁰. Su et al. also reported a significant increase in both R_{sf} and R_{ct} only for the electrode coated via 10 ALD cycles. The study by Negi et al. on a coated NMC811 electrode reported an

improved rate capability for the electrode¹⁴ but did not characterize the kinetic properties to identify the origin of such an improvement.

Discussion

The present result demonstrating only a limited benefit (i.e., slightly better stability against 1-day ambient exposure) with Al₂O₃ coating seems to contradict numerous previous studies that report significant improvement in the electrochemical performance of coated electrodes^{42,60,85,86}. Nevertheless, significant improvements in past studies are commonly observed for the surface coating/modification of homemade electrode materials, whose performance trails the commercial ones. It is worth noting that the capacity retention of the baseline electrode in the present work (160 mAh/g at 100 cycles) outperforms the Al₂O₃-coated electrode using homemade NMC811 electrode materials (160 mAh/g at 40 cycles)⁷. Even comparing with reports that adopted commercial NMC811 electrode materials^{41,70,87}, the commercial NMC811 used in the present study shows superior capacity retention. It is possible that the high-quality of the commercial NMC811 adopted in the present study renders less room for improvement in the electrochemical performance by the surface coating method.

The ALD of Al₂O₃ in the present work was performed on electrode films as opposed to electrode powders. In the ALD of electrode films, the coating is expected to be deposited on open surfaces of all components, including the NMC811 particles, the carbon additives, and the PVDF binder. Yet, it is unclear whether the deposition is homogeneous throughout the porous electrode, especially along the thickness of the electrode. To examine the spatial homogeneity of the Al₂O₃ coating, we measured the elemental distribution along the thickness of a thick NMC811 electrode coated by Al₂O₃ using ALD. The elemental mapping of the cross-section of the electrode shows a higher concentration of Al near the top layer of the composite electrode than the interior (Fig. S5), which indicates the preferential coating of only the top layer of the electrode particles. This means that coating on all NMC811 particles could be realized provided that the electrode is sufficiently thin. In this work, the electrode is ~70 μm thick (areal loading is 5.6 mg/cm²), which corresponds to 2–3 layers of NMC811 secondary particles. Hence, the deposition of the Al₂O₃ coating is expected to cover most open surface area of the electrodes, which is corroborated by both the homogeneous spatial distribution of Al and the increased surface film resistance of the coated electrodes. The reported improvement for composite electrode films coated with the ALD method also implies the successful coating of a significant fraction of the open surface in these thin, porous electrodes, e.g. 2.5 mg/cm² NMC532 electrode by Shi et al.⁶⁰, 11.6 mg/cm² NMC622 electrode by Neudeck et al.⁸⁶ and 10.8 mg/cm² NMC71515 electrode by Negi et al.⁴². Notwithstanding the widely acclaimed benefits of the surface coatings for NMC materials, the effects of the Al₂O₃ coating on Ni-rich NMCs, such as NMC811, are controversial. While Gao et al. reported improved capacity retention of both the as-prepared and the annealed (750 °C) Al₂O₃-coated polycrystalline NMC811 electrodes (Al₂O₃ coating on powder by ALD⁴¹, recent studies by Han et al.⁶³ and Riesgo-Gonzalez et al.⁶⁴ found that the high-temperature annealing of Al₂O₃-coated NMC811 particles by wet-chemical methods resulted in deteriorated capacity retention. In agreement with our result, Riesgo-Gonzalez et al.⁶⁴ observed no significant difference in the capacity retention between the pristine and the coated sample when annealed below 400 °C. This challenges the presumption that coating the electrodes with refractory materials always improves the capacity retention. Indeed, a recent work on the Al₂O₃ coatings on a LiNi_{0.5}Mn_{1.5}O₄ cathode shows aggravated electrochemical performance⁶⁶.

It has been well known that impurities, such as Li₂CO₃, readily form on the surface of NMC particles⁸⁸. The presence of such surface impurities undermines the assumption that the deposition of the Al₂O₃ coating via ALD is directly on the cathode particle surface, i.e., the transition metal oxide lattice. This assumption is further challenged when the ALD is performed on electrodes, where the surface is well covered with a layer of the polymeric binder (e.g., PVDF). The elemental mapping of the as-prepared electrode shows the spatial overlap between the F-containing species and the NMC particles, demonstrating at least partial surface coverage of the NMC811 particles with the PVDF binder, as shown in Supplementary Fig. S6. The XPS 1s measured for both the NMC811 powder and electrodes shows a suppressed peak at 529 eV (assigned to the lattice oxygen of NMC811^{78,89,90}), and a prominent peak at 532 eV (assigned to lithium carbonate^{78,89,90}) (Fig. 11). This indicates that the surface of the NMC particles is already covered with a layer of secondary species that prevents the direct reaction and bonding between the ALD precursors (i.e., TMA) and the oxide surface of NMC811. Therefore, an interlayer must exist between the Al₂O₃ coating layer and the oxide surface of the NMC811 particles (Fig. 12). Further work on Al₂O₃ coating of pristine commercial NMC811 powders is required to elucidate the effect of this interlayer on the electrochemical performance.

This brings into question the efficacy of the Al₂O₃ coating as a physical barrier to prevent the direct contact between the NMC particles and the electrolyte when the Al₂O₃ layer is not chemically bonded to the NMC oxide surface. For example, a gap between the Al₂O₃ layer and the NMC oxide surface could develop when the surface Li₂CO₃ is decomposed electrochemically during charge. This could explain the present result where the Al₂O₃ coating on the electrode does not improve electrochemical performance.

Conclusions

Electrode films prepared with commercial polycrystalline NMC811 powder were coated with Al₂O₃ by ALD to investigate the effect of surface coating on the electrode's electrochemical performance. Electrochemical characterization shows no significant differences between the coated and bare electrodes in the capacity retention at different cut-off voltages or the rate capability. The coated electrode does show improved stability against short term air exposure, where the bare electrode suffered a larger irreversible capacity loss. Yet, this improved stability is independent of the coating layer thickness and is not manifested for long-term air exposure. We speculate that the pre-existing secondary species on the NMC particle surface in the composite electrode introduces an interlayer between the NMC oxide surface and the Al₂O₃ coating layer, which undermines the efficacy of the

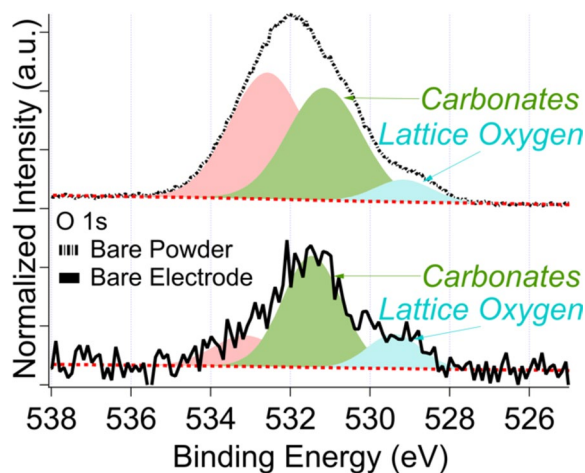


Figure 11. O 1s XPS spectra of bare NMC811 powder and bare electrode. The prominent peak at ~531 eV is attributed to surface carbonates and overshadows the lattice oxygen peak of NMC811 at 529 eV.

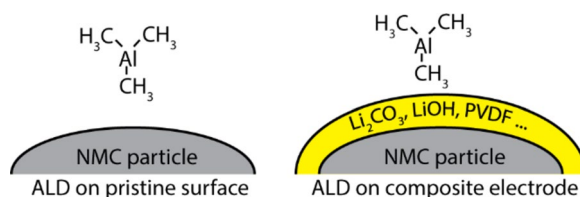


Figure 12. Illustration of the ALD on pristine NMC particle surface and on the composite electrode. The secondary species introduced during the electrode preparation step prevents the direct Al_2O_3 deposition on the NMC particle surface.

coating layer. Our work underlines the contentious effect of Al_2O_3 coating on NMC811 electrodes, which warrants further investigation.

Methods

Electrode preparation

Polycrystalline NMC811 powder purchased from Xiamen TMAX Battery Equipments was used as the active cathode material. NMC811 cathode powder (90 wt%), acetylene black (Alfa Aesar, 5 wt%) and polyvinylidene fluoride (PVDF, Sigma Aldrich, 5 wt%) were well mixed with N-methyl-2-pyrrolidone (NMP, Sigma Aldrich) to form a homogeneous slurry. The slurry cast was completed on a coating line. After drying out the NMP solvent, a roll of electrode with an areal loading of 5.6 mg/cm^2 was obtained.

ALD of Al_2O_3 on NMC811 electrode films

The Al_2O_3 coating layer was deposited on the NMC811 electrode films at 80°C in an ALD system (this temperature was selected based on the results from a few trial runs at 80°C , 100°C , 120°C and 140°C , as shown in Supplementary Fig S7). Trimethylaluminum (TMA) and water vapor was used as the precursors. High-purity N_2 gas was flowed into the chamber as the carrier of the precursors and maintained the chamber pressure of about 200 mTorr before the injection of the precursors. A complete ALD deposition cycle includes the following steps: (1) pulsing TMA for 150 ms, (2) purging the TMA residual for 20 s, (3) pulsing water for 150 ms, and (4) purging the water residual for 25 s. 2, 5, 10 and 20 ALD cycles were applied on the electrode sheets to deposit Al_2O_3 with different thickness, which are denoted as ALD-2, ALD-5, ALD-10 and ALD-20, respectively.

Coin cell assembly

The as-coated electrode was punched into discs with 14 mm diameter outside glovebox and then was transferred into glovebox for further coin cell assembly. The coin cell was assembled with a NMC811 electrode disc as the cathode, a lithium chip (1.1 mm thick and 15.4 mm in diameter, purchased from TOB) as the anode, a class fiber disc (3/4 inch, Whatman) as the separator, and electrolyte (175 μL) of 1 M LiPF_6 dissolved in 1:1 (weight ratio) dimethyl carbonate/ethylene carbonate solvent (Gotion).

Materials characterizations

The X-ray photoelectron spectroscopy (XPS) was performed on a PHI 5000 VersaProbe. Its X-ray energy was 1486 eV from Al K α line achieved by electrons bombarding the aluminum anode with 50-Watt power and 15 kV anode voltage. The X-ray spot size and pass flux was set to 200 μm and 29,350, respectively. The emission angle $\theta = 45^\circ$ to optimize the thickness measurement. The as-measured XPS spectra were calibrated by setting the graphitic carbon 1 s peak at 284.5 eV.

A ZEISS SUPRA 55-VP scanning electron microscope (SEM) was used for the secondary electron mapping and the energy-dispersive X-ray (EDX) spectroscopy of the NMC811 particles and electrodes.

Transmission electron microscopy (TEM) was used to characterize the coated electrode. NMC811 particles were collected from the ALD-2 and ALD-20 electrodes. Thin slices of TEM samples were prepared using focused ion beam (FIB) lift-out techniques to obtain clear cross-sectional views. High-angle annular dark-field (HAADF) imaging, energy-dispersive X-ray spectroscopy (EDX) with a mapping and line scan time of 900 s to ensure sufficient elemental signal acquisition, and high-resolution transmission electron microscopy (HR-TEM) images were collected using a FEI Talos F200X (200 keV) at the Center for Functional Nanomaterials at Brookhaven National Laboratory.

The X-ray powder diffraction was performed with a Bruker D8 Advance diffractometer with Mo K α radiation in the 2θ range of 5° – 55° and a scanning rate of $2^\circ/\text{min}$ (in 2θ).

Electrochemical tests

All electrochemical cycling measurements were performed on a LAND battery testing system (model CT3001A). The as-assembled cells rested for six hours before the application of the cycling protocol. For long-term cyclings, the charging protocol follows the constant current constant voltage (CCCV) charging method, where the cell was galvanostatically charged at C/3 rate to 4.4 V or 4.6 V followed by a potentiostatic charge until the current drops to C/20. Galvanostatic discharge at C/3 was used for discharge to 2.8 V. Here, 1C corresponds to 200 mA/g.

Rate tests were conducted at room temperature, within the voltage window of 2.8 V–4.2 V to minimize side reactions at high voltages. The charge protocol followed the CCCV method as described above, and the rate was varied only on discharge sequentially from C/3 to 1C, 1.5C, 2C and 3C. A recovery cycle at the rate of C/3 was performed at the end of rate test.

Potentiostatic intermittent titration technique (PITT)

PITT measurement was performed for the 2nd cycle on a Biologic BCS-805 potentiostat in voltage steps of 10 mV during both charge and discharge in the voltage window of 2.8–4.4 V. The voltage was held constant at each step until the current decreased to C/100. The chronoamperometry data ($I(t)$) for each potentiostatic step was fitted with Eq. (1) assuming a finite interfacial kinetics⁹¹,

$$I(t) = -\frac{3DQ}{r^2} \left\{ -\frac{B}{B-1} \left(1 - \operatorname{erfc} \frac{r}{\sqrt{Dt}} \right) + \frac{B^2}{B-1} e^{\frac{Dt}{r^2}(B-1)^2} \operatorname{erfc} \left[(B-1) \sqrt{\frac{Dt}{r^2}} \right] + \frac{B^2 - 2B}{B-1} e^{2(B-1) + \frac{Dt}{r^2}(B-1)^2} \operatorname{erfc} \left[\frac{r}{\sqrt{Dt}} + (B-1) \sqrt{\frac{Dt}{r^2}} \right] \right\} \quad (1)$$

where D is the Li-ion diffusivity, r the radius of the electrode particle, Q the total charge transferred during the potential step for the whole electrode, B the Biot number. Both B and D are fitting parameters. The exchange current density is derived from Eq. (2)⁹²,

$$j_0 = -\frac{BDRT}{r \frac{\partial U}{\partial C}} \quad (2)$$

where B and D are the Biot number and Li-ion diffusivity, respectively, obtained from Eq. (1), R is the universal gas constant, T is the temperature in Kelvin degree, r is the particle radius (estimated to be 13 μm), and $\frac{\partial U}{\partial C}$ is the derivative of the cell voltage (U) with respect to the Li-ion concentration (C) in the NMC particle, which is obtained from the voltage vs capacity curve for NMC.

Electrochemical impedance spectroscopy (EIS)

The EIS were measured during the discharging of the 2nd cycle from 4.4 V down to 3.8 V in steps of 100 mV on Ivium PocketStat2. The cell was equilibrated at the target voltage for 30 min before every EIS measurement. EIS data fitting was performed with the Python package of impedance.py⁹³.

Data availability

All relevant data are available from the corresponding author on reasonable request.

Received: 13 February 2024; Accepted: 2 August 2024

Published online: 06 August 2024

References

1. Hsieh, C. T. *et al.* Roll-to-roll atomic layer deposition of titania nanocoating on thermally stabilizing lithium nickel cobalt manganese oxide cathodes for lithium ion batteries. *ACS Appl. Energy Mater.* **3**, 10619–10631 (2020).

2. Su, Y. *et al.* Improving the cycling stability of Ni-rich cathode materials by fabricating surface rock salt phase. *Electrochim. Acta* **292**, 217–226 (2018).
3. Su, Y. *et al.* Enhancing the high-voltage cycling performance of $\text{LiNi}_{0.5}\text{Mn}_{0.3}\text{Co}_{0.2}\text{O}_2$ by retarding its interfacial reaction with an electrolyte by atomic-layer-deposited Al_2O_3 . *ACS Appl. Mater. Interfaces* **7**, 25105–25112 (2015).
4. Li, W. *et al.* Long-term cyclability of NCM-811 at high voltages in lithium-ion batteries: An in-depth diagnostic study. *Chem. Mater.* **32**, 7796–7804 (2020).
5. Xu, C. *et al.* Bulk fatigue induced by surface reconstruction in layered Ni-rich cathodes for Li-ion batteries. *Nat. Mater.* **20**, 84–92 (2021).
6. Sallis, S. *et al.* Surface degradation of $\text{Li}_{1-x}\text{Ni}_{0.80}\text{Co}_{0.15}\text{Al}_{0.05}\text{O}_2$ cathodes: Correlating charge transfer impedance with surface phase transformations. *Appl. Phys. Lett.* **108**, 1–5 (2016).
7. Pei, B. *et al.* Al substitution for Mn during co-precipitation boosts the electrochemical performance of $\text{LiNi}_{0.8}\text{Mn}_{0.1}\text{Co}_{0.1}\text{O}_2$. *J. Electrochem. Soc.* **168**, 050532 (2021).
8. Croy, J. R. *et al.* Insights on the stabilization of nickel-rich cathode surfaces: Evidence of inherent instabilities in the presence of conformal coatings. *Chem. Mater.* **31**, 2–10. <https://doi.org/10.1021/acs.chemmater.8b04332> (2019).
9. Tebbe, J. L., Holder, A. M. & Musgrave, C. B. Mechanisms of LiCoO_2 cathode degradation by reaction with HF and protection by thin oxide coatings. *ACS Appl. Mater. Interfaces* **7**, 24265–24278 (2015).
10. Liu, T. *et al.* Correlation between manganese dissolution and dynamic phase stability in spinel-based lithium-ion battery. *Nat. Commun.* **10**, 4721 (2019).
11. Lim, S. N., Ahn, W., Yeon, S. H. & Park, S. B. Enhanced elevated-temperature performance of $\text{Li}(\text{Ni}_{0.8}\text{Co}_{0.15}\text{Al}_{0.05})\text{O}_2$ electrodes coated with $\text{Li}_2\text{O}-2\text{B}_2\text{O}_3$ glass. *Electrochim. Acta* **136**, 1–9 (2014).
12. Faenza, N. V. *et al.* Electrolyte-induced surface transformation and transition-metal dissolution of fully delithiated $\text{LiNi}_{0.8}\text{Co}_{0.15}\text{Al}_{0.05}\text{O}_2$. *Langmuir* **33**, 9333–9353 (2017).
13. Schultz, C., Vedder, S., Streipert, B., Winter, M. & Nowak, S. Quantitative investigation of the decomposition of organic lithium ion battery electrolytes with LC-MS/MS. *RSC Adv.* **7**, 27853–27862 (2017).
14. Negi, R. S. *et al.* Optimized atomic layer deposition of homogeneous, conductive Al_2O_3 coatings for high-nickel NCM containing ready-to-use electrodes. *Phys. Chem. Chem. Phys.* **23**, 6725–6737 (2021).
15. Myung, S. T. *et al.* Role of alumina coating on Li-Ni-Co-Mn-O particles as positive electrode material for lithium-ion batteries. *Chem. Mater.* **17**, 3695–3704 (2005).
16. Xin, F. *et al.* Li-Nb-O coating/substitution enhances the electrochemical performance of the $\text{LiNi}_{0.8}\text{Mn}_{0.1}\text{Co}_{0.1}\text{O}_2$ (NMC 811) cathode. *ACS Appl. Mater. Interfaces* **11**, 34889–34894 (2019).
17. Zhang, X., Cui, Z. & Manthiram, A. Insights into the crossover effects in cells with high-nickel layered oxide cathodes and silicon/graphite composite anodes. *Adv. Energy Mater.* **2103611**, 1–9 (2022).
18. Yi, M., Li, W. & Manthiram, A. Delineating the roles of Mn, Al, and Co by comparing three layered oxide cathodes with the same nickel content of 70% for lithium-ion batteries. *Chem. Mater.* **34**, 629–642 (2022).
19. Sharma, L., Yi, M., Jo, E., Celio, H. & Manthiram, A. Surface stabilization with fluorine of layered ultrahigh-nickel oxide cathodes for lithium-ion batteries. *Chem. Mater.* <https://doi.org/10.1021/acs.chemmater.2c00301> (2022).
20. Liu, J. *et al.* Pathways for practical high-energy long-cycling lithium metal batteries. *Nat. Energy* **4**, 180–186 (2019).
21. Choi, J. U., Voronina, N., Sun, Y. K. & Myung, S. T. Recent progress and perspective of advanced high-energy Co-less Ni-rich cathodes for Li-ion batteries: Yesterday, today, and tomorrow. *Adv. Energy Mater.* **10**, 1–31 (2020).
22. Friedrich, F. *et al.* Editors' choice—Capacity fading mechanisms of NCM-811 cathodes in lithium-ion batteries studied by X-ray diffraction and other diagnostics. *J. Electrochem. Soc.* **166**, A3760–A3774 (2019).
23. Zhu, J. *et al.* Investigation of lithium-ion battery degradation mechanisms by combining differential voltage analysis and alternating current impedance. *J. Power Sources* **448**, 227575 (2020).
24. Zhang, H. & Zhang, J. An overview of modification strategies to improve $\text{LiNi}_{0.8}\text{Co}_{0.1}\text{Mn}_{0.1}\text{O}_2$ (NMC811) cathode performance for automotive lithium-ion batteries. *eTransportation* **7**, 100105 (2021).
25. Muruganatham, R., Tseng, T. H., Lee, M. L., Kheawhom, S. & Liu, W. R. Artificial interface modification of Ni-rich ternary cathode material to enhance electrochemical performance for Li-ion storage through RF-plasma-assisted technique. *Chem. Eng. J.* **464**, 142686 (2023).
26. Fan, Q. *et al.* Surface Reduction Stabilizes the Single-Crystalline Ni-Rich Layered Cathode for Li-Ion Batteries. *ACS Appl. Mater. Interfaces* **14**, 38795–38806 (2022).
27. Xin, F. *et al.* What is the Role of Nb in Nickel-Rich Layered Oxide Cathodes for Lithium-Ion Batteries?. *ACS Energy Lett.* **6**, 1377–1382 (2021).
28. Zhang, N. *et al.* Effects of Fluorine Doping on Nickel-Rich Positive Electrode Materials for Lithium-Ion Batteries. *J. Electrochem. Soc.* **167**, 080518 (2020).
29. Zaker, N. *et al.* Probing the mysterious behavior of tungsten as a dopant inside pristine cobalt-free nickel-rich cathode materials. *Adv. Funct. Mater.* <https://doi.org/10.1002/adfm.202211178> (2023).
30. Sun, Y. K. *et al.* A novel cathode material with a concentration gradient for high-energy and safe Lithium-Ion batteries. *Adv. Funct. Mater.* **20**, 485–491 (2010).
31. Sun, Y. K. *et al.* A novel concentration-gradient $\text{Li}[\text{Ni}_{0.83}\text{Co}_{0.07}\text{Mn}_{0.10}]\text{O}_2$ cathode material for high-energy lithium-ion batteries. *J. Mater. Chem.* **21**, 10108–10112 (2011).
32. Park, K. J. *et al.* A high-capacity $\text{Li}[\text{Ni}_{0.8}\text{Co}_{0.06}\text{Mn}_{0.14}]\text{O}_2$ positive electrode with a dual concentration gradient for next-generation lithium-ion batteries. *J. Mater. Chem. A* **3**, 22183–22190 (2015).
33. Sun, Y. K., Kim, D. H., Jung, H. G., Myung, S. T. & Amine, K. High-voltage performance of concentration-gradient $\text{Li}[\text{Ni}_{0.67}\text{Co}_{0.15}\text{Mn}_{0.18}]\text{O}_2$ cathode material for lithium-ion batteries. *Electrochim. Acta* **55**, 8621–8627 (2010).
34. Liu, T. *et al.* Rational design of mechanically robust Ni-rich cathode materials via concentration gradient strategy. *Nat. Commun.* **12**, 1 (2021).
35. Li, Y. *et al.* Synthesis of full concentration gradient cathode studied by high energy X-ray diffraction. *Nano Energy* **19**, 522–531 (2016).
36. Hemmelmann, H., Dinter, J. K. & Elm, M. T. Thin Film NCM cathodes as model systems to assess the influence of coating layers on the electrochemical performance of lithium ion batteries. *Adv. Mater. Interfaces* **8**, 2074 (2021).
37. Liu, S. *et al.* Comparative studies of zirconium doping and coating on $\text{LiNi}_{0.6}\text{Co}_{0.2}\text{Mn}_{0.2}\text{O}_2$ cathode material at elevated temperatures. *J. Power Sources* **396**, 288–296 (2018).
38. Han, B. *et al.* Influence of coating protocols on alumina-coated cathode material: Atomic layer deposition versus wet-chemical coating. *J. Electrochem. Soc.* **166**, A3679–A3684 (2019).
39. Becker, D. *et al.* Surface modification of Ni-rich $\text{LiNi}_{0.8}\text{Co}_{0.1}\text{Mn}_{0.1}\text{O}_2$ cathode material by tungsten oxide coating for improved electrochemical performance in lithium-ion batteries. *ACS Appl. Mater. Interfaces* **11**, 18404–18414 (2019).
40. Zhang, H., Xu, J. & Zhang, J. Surface-coated $\text{LiNi}_{0.8}\text{Co}_{0.1}\text{Mn}_{0.1}\text{O}_2$ (NMC811) cathode materials by Al_2O_3 , ZrO_2 , and $\text{Li}_2\text{O}-2\text{B}_2\text{O}_3$ thin-layers for improving the performance of lithium ion batteries. *Front. Mater.* **6**, 1–10 (2019).
41. Gao, Y., Park, J. & Liang, X. Comprehensive study of Al- And Zr-modified $\text{LiNi}_{0.8}\text{Mn}_{0.1}\text{Co}_{0.1}\text{O}_2$ through synergy of coating and doping. *ACS Appl. Energy Mater.* **3**, 8978–8987 (2020).

42. Negi, R. S., Culver, S. P., Mazilkin, A., Brezesinski, T. & Elm, M. T. Enhancing the electrochemical performance of $\text{LiNi}_{0.70}\text{Co}_{0.15}\text{Mn}_{0.15}\text{O}_2$ cathodes using a practical solution-based Al_2O_3 coating. *ACS Appl. Mater. Interfaces* **12**, 31392–31400 (2020).
43. Wu, F. *et al.* Dual-anion ionic liquid electrolyte enables stable Ni-rich cathodes in lithium-metal batteries. *Joule* **5**, 2177–2194 (2021).
44. Li, J. *et al.* The impact of electrolyte additives and upper cut-off voltage on the formation of a rocksalt surface layer in $\text{LiNi}_{0.8}\text{Mn}_{0.1}\text{Co}_{0.1}\text{O}_2$ electrodes. *J. Electrochem. Soc.* **164**, A655–A665 (2017).
45. Pender, J. P. *et al.* Electrode degradation in lithium-ion batteries. *ACS Nano* **14**, 1243–1295 (2020).
46. Neudeck, S. *et al.* Room temperature, liquid-phase Al_2O_3 surface coating approach for Ni-rich layered oxide cathode material. *Chem. Commun.* **55**, 2174–2177 (2019).
47. Wang, J. *et al.* Providing a long-term protection for NCM811 cathode material by Al_2O_3 coating layer. *IOP Conf. Ser. Mater. Sci. Eng.* **735**, 012007 (2020).
48. Feng, Y. *et al.* Enhanced electrochemical performance of $\text{LiNi}_{0.8}\text{Co}_{0.1}\text{Mn}_{0.1}\text{O}_2$ cathode materials by Al_2O_3 coating. *J. Electrochem. Energy Convers. Storage* **18**, 1 (2020).
49. Hu, D. *et al.* An effective strategy to control thickness of Al_2O_3 coating layer on nickel-rich cathode materials. *J. Electroanal. Chem.* **880**, 114910 (2021).
50. Xiao, L., Davenport, D. M., Ormsbee, L. & Bhattacharyya, D. Polymerization and functionalization of membrane pores for water related applications. *Ind. Eng. Chem. Res.* **54**, 4174–4182 (2015).
51. Wang, X. *et al.* Atomic-scale constituting stable interface for improved $\text{LiNi}_{0.6}\text{Mn}_{0.2}\text{Co}_{0.2}\text{O}_2$ cathodes of lithium-ion batteries. *Nanotechnology* **32**, 1154 (2021).
52. Zhu, W. *et al.* Ultrathin Al_2O_3 coating on $\text{LiNi}_{0.8}\text{Co}_{0.1}\text{Mn}_{0.1}\text{O}_2$ cathode material for enhanced cycleability at extended voltage ranges. *Coatings* **9**, 1–12 (2019).
53. Ramasamy, H. V. *et al.* Enhancement of electrochemical activity of Ni-rich $\text{LiNi}_{0.8}\text{Mn}_{0.1}\text{Co}_{0.1}\text{O}_2$ by precisely controlled Al_2O_3 nanocoatings via atomic layer deposition. *J. Electrochem. Sci. Technol.* **10**, 196–205 (2019).
54. Wang, L. *et al.* Optimized structure stability and cycling performance of $\text{LiNi}_{0.8}\text{Co}_{0.1}\text{Mn}_{0.1}\text{O}_2$ through homogeneous nano-thickness Al_2O_3 coating. *Electrochim. Acta* **435**, 141411 (2022).
55. Kim, J. H. *et al.* Stabilizing the surface of Ni-rich cathodes via facing-target sputtering for high-performance lithium-ion batteries. *J. Mater. Chem. A* **10**, 25009–25018 (2022).
56. Dong, M. *et al.* Metallurgy inspired formation of homogeneous Al_2O_3 coating layer to improve the electrochemical properties of $\text{LiNi}_{0.8}\text{Co}_{0.1}\text{Mn}_{0.1}\text{O}_2$ cathode material. *ACS Sustain. Chem. Eng.* **5**, 10199–10205 (2017).
57. Kimura, N., Seki, E., Tooyama, T. & Nishimura, S. STEM-EELS analysis of improved cycle life of lithium-ion cells with Al_2O_3 -coated $\text{LiNi}_{0.8}\text{Co}_{0.1}\text{Mn}_{0.1}\text{O}_2$ cathode active material. *J. Alloys Compd.* **869**, 159259 (2021).
58. Srimanon, K., Vadivel, S. & Sawangphruk, M. Inhibition of Gas-evolved electrolyte decomposition in cylindrical Li-ion battery cells of Ni-rich layered oxide with a dry coating process without post thermal annealing. *J. Power Sources* **550**, 232150 (2022).
59. King, D. M., Liang, X. & Weimer, A. W. Functionalization of fine particles using atomic and molecular layer deposition. *Powder Technol.* **221**, 13–25 (2012).
60. Shi, Y., Zhang, M., Qian, D. & Meng, Y. S. Ultrathin Al_2O_3 coatings for improved cycling performance and thermal stability of $\text{LiNi}_{0.5}\text{Co}_{0.2}\text{Mn}_{0.3}\text{O}_2$ cathode material. *Electrochim. Acta* **203**, 154–161 (2016).
61. Park, J. S., Mane, A. U., Elam, J. W. & Croy, J. R. Atomic layer deposition of Al-W-fluoride on LiCoO_2 cathodes: Comparison of particle- and electrode-level coatings. *ACS Omega* **2**, 3724–3729 (2017).
62. Bao, W. *et al.* Simultaneous enhancement of interfacial stability and kinetics of single-crystal $\text{LiNi}_{0.6}\text{Mn}_{0.2}\text{Co}_{0.2}\text{O}_2$ through optimized surface coating and doping. *Nano Lett.* **20**, 8832–8840 (2020).
63. Han, B. *et al.* From coating to dopant: How the transition metal composition affects alumina coatings on Ni-rich cathodes. *ACS Appl. Mater. Interfaces* **9**, 41291–41302 (2017).
64. Riesgo-González, V. *et al.* Effect of annealing on the structure, composition, and electrochemistry of NMC811 coated with Al_2O_3 using an alkoxide precursor. *Chem. Mater.* **34**, 9722–9735 (2022).
65. Yu, H., Gao, Y. & Liang, X. Slightly fluorination of Al_2O_3 ALD coating on $\text{Li}_{1.2}\text{Mn}_{0.54}\text{Co}_{0.13}\text{Ni}_{0.13}\text{O}_2$ electrodes: Interface reaction to create stable solid permeable interphase layer. *J. Electrochem. Soc.* **166**, A2021–A2027 (2019).
66. Østli, E. R. *et al.* Limitations of ultrathin Al_2O_3 coatings on LNMO cathodes. *ACS Omega* **6**, 30644–30655 (2021).
67. Younesi, R. *et al.* Analysis of the interphase on carbon black formed in high voltage batteries. *J. Electrochem. Soc.* **162**, A1289–A1296 (2015).
68. Kim, Y. C., Park, H. H., Chun, J. S. & Lee, W. J. Compositional and structural analysis of aluminum oxide films prepared by plasma-enhanced chemical vapor deposition. *Thin Solid Films* **237**, 57–65 (1994).
69. Zhou, H., Xin, F., Pei, B. & Whittingham, M. S. What limits the capacity of layered oxide cathodes in lithium batteries?. *ACS Energy Lett.* **4**, 1902–1906 (2019).
70. Dong, Q. *et al.* Insights into the dual role of lithium difluoro(oxalato)borate additive in improving the electrochemical performance of NMC811||graphite cells. *ACS Appl. Energy Mater.* **3**, 695–704 (2020).
71. Savina, A. A. & Abakumov, A. M. Benchmarking the electrochemical parameters of the $\text{LiNi}_{0.8}\text{Mn}_{0.1}\text{Co}_{0.1}\text{O}_2$ positive electrode material for Li-ion batteries. *Heliyon* **9**, e21881 (2023).
72. Thapaliya, B. P. *et al.* Enhancing cycling stability and capacity retention of NMC811 cathodes by reengineering interfaces via electrochemical fluorination. *Adv. Mater. Interfaces* **9**, 2200035 (2022).
73. Sim, R., Lee, S., Li, W. & Manthiram, A. Influence of calendaring on the electrochemical performance of $\text{LiNi}_{0.9}\text{Mn}_{0.05}\text{Al}_{0.05}\text{O}_2$ cathodes in lithium-ion cells. *ACS Appl. Mater. Interfaces* **13**, 42898–42908 (2021).
74. Jung, R., Metzger, M., Maglia, F., Stinner, C. & Gasteiger, H. A. Chemical versus electrochemical electrolyte oxidation on NMC111, NMC622, NMC811, LNMO, and conductive carbon. *J. Phys. Chem. Lett.* **8**, 4820–4825 (2017).
75. Dose, W. M. *et al.* Onset potential for electrolyte oxidation and Ni-rich cathode degradation in lithium-ion batteries. *ACS Energy Lett.* **7**, 3524–3530 (2022).
76. Ou, X. *et al.* Enabling high energy lithium metal batteries via single-crystal Ni-rich cathode material co-doping strategy. *Nat. Commun.* **13**, 2319 (2022).
77. Sicklinger, J., Metzger, M., Beyer, H., Pritzl, D. & Gasteiger, H. A. Ambient storage derived surface contamination of NCM811 and NCM111: Performance implications and mitigation strategies. *J. Electrochem. Soc.* **166**, A2322–A2335 (2019).
78. You, Y., Celio, H., Li, J., Dolocan, A. & Manthiram, A. Modified high-nickel cathodes with stable surface chemistry against ambient air for lithium-ion batteries. *Angew. Chem.* **130**, 6590–6595 (2018).
79. Grenier, A. *et al.* Reaction heterogeneity in $\text{LiNi}_{0.8}\text{Co}_{0.15}\text{Al}_{0.05}\text{O}_2$ induced by surface layer. *Chem. Mater.* **29**, 7345–7352 (2017).
80. McClelland, I. *et al.* Direct observation of dynamic lithium diffusion behavior in nickel-rich, $\text{LiNi}_{0.8}\text{Mn}_{0.1}\text{Co}_{0.1}\text{O}_2$ (NMC811) cathodes using operando muon spectroscopy. *Chem. Mater.* **2**, 0–9 (2022).
81. Märker, K., Reeves, P. J., Xu, C., Griffith, K. J. & Grey, C. P. Evolution of structure and lithium dynamics in $\text{LiNi}_{0.8}\text{Mn}_{0.1}\text{Co}_{0.1}\text{O}_2$ (NMC811) cathodes during electrochemical cycling. *Chem. Mater.* **31**, 2545–2554 (2019).
82. Min, J., Gubow, L. M., Hargrave, R. J., Siegel, J. B. & Li, Y. Direct measurements of size-independent lithium diffusion and reaction times in individual polycrystalline battery particles. *Energy Environ. Sci.* **16**, 6–17. <https://doi.org/10.1039/D3EE00953J> (2023).
83. Trevisanello, E., Ruess, R., Conforto, G., Richter, F. H. & Janek, J. Polycrystalline and single crystalline NCM cathode materials—Quantifying particle cracking, active surface area, and lithium diffusion. *Adv. Energy Mater.* **11**, 2003400 (2021).

84. Dose, W. M. *et al.* Electrolyte reactivity at the charged Ni-rich cathode interface and degradation in Li-ion batteries. *ACS Appl. Mater. Interfaces* <https://doi.org/10.1021/acsami.1c22812> (2022).
85. Lee, J. T., Wang, F. M., Cheng, C. S., Li, C. C. & Lin, C. H. Low-temperature atomic layer deposited Al₂O₃ thin film on layer structure cathode for enhanced cycleability in lithium-ion batteries. *Electrochim. Acta* **55**, 4002–4006 (2010).
86. Neudeck, S. *et al.* Effect of low-temperature Al₂O₃ ALD coating on Ni-rich layered oxide composite cathode on the long-term cycling performance of lithium-ion batteries. *Sci. Rep.* **9**, 1–11 (2019).
87. Mohanty, D. *et al.* Modification of Ni-Rich FCG NMC and NCA cathodes by atomic layer deposition: Preventing surface phase transitions for high-voltage lithium-ion batteries. *Sci. Rep.* **6**, 1–16 (2016).
88. Hatsukade, T., Schiele, A., Hartmann, P., Brezesinski, T. & Janek, J. Origin of carbon dioxide evolved during cycling of nickel-rich layered NCM cathodes. *ACS Appl. Mater. Interfaces* **10**, 38892–38899 (2018).
89. Faenza, N. V. *et al.* Growth of ambient induced surface impurity species on layered positive electrode materials and impact on electrochemical performance. *J. Electrochem. Soc.* **164**, A3727–A3741 (2017).
90. de Meazza, I. *et al.* Influence of the ambient storage of LiNi_{0.8}Mn_{0.1}Co_{0.1}O₂ powder and electrodes on the electrochemical performance in Li-ion technology. *Batteries* **8**, 79 (2022).
91. Li, J., Yang, F., Xiao, X., Verbrugge, M. W. & Cheng, Y. T. Potentiostatic intermittent titration technique (PITT) for spherical particles with finite interfacial kinetics. *Electrochim. Acta* **75**, 56–61 (2012).
92. Tsai, P. C. *et al.* Single-particle measurements of electrochemical kinetics in NMC and NCA cathodes for Li-ion batteries. *Energy Environ. Sci.* **11**, 860–871 (2018).
93. Murbach, M., Gerwe, B., Dawson-Elli, N. & Tsui, L. impedance.py: A Python package for electrochemical impedance analysis. *J. Open Source Softw.* **5**, 2349 (2020).

Acknowledgements

This work was funded by the National Science Foundation CBET-2028722. L.Q. and G.Z. acknowledge the support by the U.S. Department of Energy (DOE), Office of Basic Energy Sciences, Division of Materials Sciences and Engineering under Award No. DE-SC0001135. This research used the Electron Microscopy Facilities of the Center for Functional Nanomaterials, which are U.S. DOE Office of Science User Facilities, at Brookhaven National Laboratory under Contract No. DE-SC0012704.

Author contributions

H.H. prepared cells, cycled cells, measured the EIS, measured the PITT, characterized SEM, EDX, XRD and XPS, processed XRD and XPS data and wrote the manuscript. L.Q. and G.Z. performed the TEM measurement. H.Z. prepared bare NMC811 composite electrode films. Y.T., P.L. and Haodong Liu applied Al₂O₃ coating onto bare NMC811 electrode via ALD. M.J.W. characterized XPS. M.S. co-supervised the project. Hao Liu processed PITT data and EIS data, wrote the manuscript and co-supervised the project. All authors reviewed and approved the manuscript.

Competing interests

The authors declare no competing interests.

Additional information

Supplementary Information The online version contains supplementary material available at <https://doi.org/10.1038/s41598-024-69330-6>.

Correspondence and requests for materials should be addressed to H.L.

Reprints and permissions information is available at www.nature.com/reprints.

Publisher's note Springer Nature remains neutral with regard to jurisdictional claims in published maps and institutional affiliations.

Open Access This article is licensed under a Creative Commons Attribution-NonCommercial-NoDerivatives 4.0 International License, which permits any non-commercial use, sharing, distribution and reproduction in any medium or format, as long as you give appropriate credit to the original author(s) and the source, provide a link to the Creative Commons licence, and indicate if you modified the licensed material. You do not have permission under this licence to share adapted material derived from this article or parts of it. The images or other third party material in this article are included in the article's Creative Commons licence, unless indicated otherwise in a credit line to the material. If material is not included in the article's Creative Commons licence and your intended use is not permitted by statutory regulation or exceeds the permitted use, you will need to obtain permission directly from the copyright holder. To view a copy of this licence, visit <http://creativecommons.org/licenses/by-nc-nd/4.0/>.

© The Author(s) 2024